

# Deblurring and Sparse Unmixing for Hyperspectral Images

Xi-Le Zhao, Fan Wang, Ting-Zhu Huang, Michael K. Ng, and Robert J. Plemmons

**Abstract**—The main aim of this paper is to study total variation (TV) regularization in deblurring and sparse unmixing of hyperspectral images. In the model, we also incorporate blurring operators for dealing with blurring effects, particularly blurring operators for hyperspectral imaging whose point spread functions are generally system dependent and formed from axial optical aberrations in the acquisition system. An alternating direction method is developed to solve the resulting optimization problem efficiently. According to the structure of the TV regularization and sparse unmixing in the model, the convergence of the alternating direction method can be guaranteed. Experimental results are reported to demonstrate the effectiveness of the TV and sparsity model and the efficiency of the proposed numerical scheme, and the method is compared to the recent Sparse Unmixing via variable Splitting Augmented Lagrangian and TV method by Iordache *et al.*

**Index Terms**—Alternating direction methods, deblurring, hyperspectral imaging, linear spectral unmixing, total variation (TV).

## I. INTRODUCTION

**H**YPERSPECTRAL sensors collect multiple images of a scene using hundreds of contiguous spectral bands from ultraviolet to visible to infrared. There are a wide range of applications such as remote surveillance, military target discrimination, medicine, astrophysics, and environmental monitoring, e.g., [1] and [2]. Many data analysis methods have been proposed and developed for hyperspectral images, for instance, classification, clustering, and spectral unmixing

[3]–[8]. In these methods, one is often interested in determining the underlying materials in each pixel. By assuming that the measured spectrum of each mixed pixel is a linear combination of spectral signatures (called endmembers), the linear spectral mixture model can be formulated as follows:

$$Y = XA + N \quad (1)$$

where the matrix  $A \in \mathbb{R}^{m \times l}$  ( $m$  is usually larger than  $l$ ) represents a spectral library containing  $m$  spectral signatures with  $l$  spectral bands,  $Y \in \mathbb{R}^{n \times l}$  is the observed data matrix (each row contains the observed spectrum of a given pixel),  $X \in \mathbb{R}^{n \times m}$  is the fractional abundance matrix of endmembers (each column contains the fractional abundances of a given endmember), and  $N \in \mathbb{R}^{n \times l}$  is the matrix collecting the errors or noise affecting the measurements at each spectral band. In the following discussion, we denote the  $(i, j)$ th entry of a matrix  $M$  by  $M_{i,j}$  or  $(M)_{i,j}$ .

Given the matrices  $Y$  and  $A$ , our purpose is to find the endmembers present in pixels, i.e., to determine the matrix  $X$ . In the literature, the abundance nonnegativity constraint  $X \geq 0$  (i.e., each entry is nonnegative) and the abundance sum-to-one constraint

$$\sum_{j=1}^m X_{i,j} = 1, \quad i = 1, \dots, n$$

are generally imposed on the fractional abundances [8].

There are several traditional methods used for such unmixing, including nonnegatively constrained least squares method, pure-pixel-based algorithms (e.g., N-FINDR [9]), minimum-volume-based algorithms (e.g., Simplex Identification via Split Augmented Lagrangian [10]), and statistical algorithms [11] to determine the fractional abundances; see [8] for a detailed discussion. Recently, several new unmixing methods based on compressed sensing have been developed and studied, see, e.g., [6], [12], [17], [19], [20], [23], [24], and [26].

Gillis and Plemmons [17], [18] have proposed the use of nonnegative matrix underapproximation to extract features in a recursive way so that hyperspectral data can be compressively represented. They also used a sparsity constraint to extract materials in each pixel [18]. In [19], Guo *et al.* studied  $l_1$  unmixing model and developed fast computational approaches based on Bregman iterations. In [12], Bioucas-Dias and Figueiredo studied alternating direction algorithms for constrained sparse regression for hyperspectral unmixing. In [6], Iordache *et al.* studied and compared several available and new linear sparse regression algorithms to solve the spectral

Manuscript received May 19, 2012; revised October 6, 2012; accepted November 1, 2012. Date of publication January 29, 2013; date of current version June 20, 2013. The work of M. K. Ng was supported by the Hong Kong Research Grant Council and Hong Kong Baptist University Faculty Research Grant. The work of X.-L. Zhao and T.-Z. Huang was supported in part by the National Natural Science Foundation of China under Grant 61170311, by the Chinese Universities Specialized Research Fund for the Doctoral Program under Grant 20110185110020, and by the Sichuan Province Science and Technology Research Project under Grants 2011JY0002 and 12ZC1802. The work of R. J. Plemmons was supported in part by the U.S. Air Force Office of Scientific Research, under Grant FA9550-11-1-0194, and in part by the U.S. National Geospatial-Intelligence Agency under Contract HM1582-10-C-0011. (Corresponding author: M. K. Ng.)

X.-L. Zhao and T.-Z. Huang are with the School of Mathematical Sciences, University of Electronic Science and Technology of China, Chengdu 610054, China (e-mail: xlzhao122003@163.com; tingzhuang@126.com).

F. Wang is with the Department of Mathematics and Statistics, Lanzhou University, Lanzhou, China (e-mail: 09466029@hkbk.edu.cn).

M. K. Ng is with the Centre for Mathematical Imaging and Vision and the Department of Mathematics, Hong Kong Baptist University, Kowloon Tong, Hong Kong (e-mail: mng@math.hkbu.edu.hk).

R. J. Plemmons is with the Department of Computer Science and the Department of Mathematics, Wake Forest University, Winston-Salem, NC 27106 USA (e-mail: plemmons@wfu.edu).

Color versions of one or more of the figures in this paper are available online at <http://ieeexplore.ieee.org>.

Digital Object Identifier 10.1109/TGRS.2012.2227764

unmixing problem by resorting to available spectral libraries. In [23], Li *et al.* developed a total variation (TV)-based method to couple the segmentation with a hyperspectral image data denoising/deblurring model. Numerical results have shown the effectiveness of the proposed combined model in hyperspectral material identification. In [24], Li *et al.* proposed a numerical procedure to compute directly the unmixed fractional abundances of given endmembers by minimizing the TV of the fractional abundances. Both synthetic and hardware-measured data are presented to demonstrate the feasibility and efficiency of the proposed approach. In [26], Zhang *et al.* developed a joint reconstruction and segmentation model for hyperspectral data obtained from a compressive measurement system, and tests on real data from a coded aperture snapshot spectral imaging camera developed by them are described.

In [6], [12], [17], and [19], sparsity constraints are considered in their models. In [23] and [24], TV regularization is incorporated. However, both are not studied together in the spectral unmixing problem, except the work given by Iordache *et al.* [20]–[22]. In [21], the authors developed a TV and sparsity regularization to the classical sparse regression in order to exploit the spatial contextual information present in the hyperspectral images. Their sparse unmixing algorithm, i.e., Sparse Unmixing via variable Splitting Augmented Lagrangian and TV (SUnSAL-TV), will be used for comparisons with our method.

The main aim of this paper is to study a TV regularization method in deblurring and sparse hyperspectral unmixing

$$\min_{X \geq 0} \frac{1}{2} \|HXA - Y\|_F^2 + \mu_1 \|X\|_{1,1} + \mu_2 \text{TV}(X) \quad (2)$$

where  $H$  is an  $n$ -by- $n$  hyperspectral data acquisition blurring matrix and  $\mu_1$  and  $\mu_2$  are two positive regularization parameters used to control the importance of the sparsity term and the TV term, respectively. Here

$$\|X\|_{1,1} := \sum_{i=1}^n \sum_{j=1}^m |X_{i,j}|.$$

The purpose for the choice of this sparsity term is that there are only a few endmembers associated with each pixel in the model. In dealing with hyperspectral data, there are other forms of TV regularization that can be employed. For instance, in [20] and [21], the following TV measure on  $X$  is used:

$$\text{TV}_a(X) := \sum_{i=1}^n \sum_{j=1}^m (|D_{i,1}\mathbf{x}_j| + |D_{i,2}\mathbf{x}_j|) \quad (3)$$

where  $\mathbf{x}_j$  refers to the  $j$ th column of  $X$ ,  $D_{i,1}\mathbf{x}_j$  and  $D_{i,2}\mathbf{x}_j$  are the gradient values of  $\mathbf{x}_j$  at the  $x$ - and  $y$ -directions of the  $i$ th pixel in the hyperspectral image, and  $D_{i,1}$  and  $D_{i,2}$  are the corresponding discrete gradient operators in the  $x$ - and  $y$ -directions, respectively. In [24], the following TV measure on  $X$  is used:

$$\text{TV}_i(X) := \sum_{i=1}^n \sum_{j=1}^m \sqrt{|D_{i,1}\mathbf{x}_j|^2 + |D_{i,2}\mathbf{x}_j|^2}. \quad (4)$$

The first measure in (3) refers to anisotropic TV, and the second measure in (4) refers to isotropic TV.

The blurring matrix  $H$  is constructed from the point spread function (PSF) and possibly imposed boundary conditions. A variety of advanced techniques are available for estimating the PSFs from spatially blurred images [28], [29]. However, the estimation of hyperspectral PSFs is generally “system dependent” [13], [30], [31]. In [13], the authors develop a model of the PSF as a “linear combination of Gaussian functions” across the spectral bands. In the experiments of this paper, for simplicity, we assume that the PSF is a single Gaussian function, and the general case is left to future work; see the remarks in Section IV. One can see that, if  $H = I$ , then the objective function (2) reduces to the one introduced in [20] and [21].

There are two main contributions in this paper.

- 1) We develop an alternating direction method to solve the optimization problem (2) efficiently. According to the structure of the TV regularization and sparse unmixing in the model, the convergence of the alternating direction method can also be guaranteed. Both anisotropic TV in (3) and isotropic TV in (4) are studied and tested for deblurring and sparse unmixing of hyperspectral data. Numerical examples are given to demonstrate the effectiveness of the model (2) and the efficiency of the proposed numerical scheme. In particular, the performance of the proposed numerical scheme appears to be better than the SUnSAL-TV method [21] which employs anisotropic TV (as mentioned in [21]), in terms of computational time and storage.
- 2) We incorporate a blurring operator in (2). However, for the SUnSAL-TV method [21], it would be required to add more auxiliary variables and computational steps in order to solve the resulting optimization problem.

The outline of this paper is given as follows. In Section II, we present our alternating direction method for deblurring and unmixing of hyperspectral images. In Section III, experimental results are reported. Finally, some conclusions are drawn in Section IV.

## II. PROPOSED NUMERICAL SCHEME

In this section, we first develop the numerical scheme for (2) by using isotropic TV. We rewrite the problem (2) as follows:

$$\min_{V, W, X} \mu_2 \sum_{i=1}^n \sum_{j=1}^m \|W_{i,j}\|_2 + \mu_1 \|V\|_{1,1} + \frac{1}{2} \|HXA - Y\|_F^2$$

subject to

$$\begin{aligned} D_1 X &= W^{(1)} & D_2 X &= W^{(2)} & V &= X \\ V &\in \mathcal{K} := \{V \in \mathbb{R}^{n \times m}, V \geq 0\} \end{aligned} \quad (5)$$

where  $W_{i,j} = [W_{i,j}^{(1)}, W_{i,j}^{(2)}] \in \mathbb{R}^{1 \times 2}$ ,  $W_{i,j}^{(1)} = D_{i,1}\mathbf{x}_j$ ,  $W_{i,j}^{(2)} = D_{i,2}\mathbf{x}_j$ ,  $1 \leq i \leq n$ ,  $1 \leq j \leq m$ , and the  $(i, j)$ th entries of  $W^{(1)}$  and  $W^{(2)}$  are given by  $W_{i,j}^{(1)}$  and  $W_{i,j}^{(2)}$ , respectively. Moreover,  $D_1$  and  $D_2$  refer to the assembled first-order difference matrices in the  $x$ - and  $y$ -directions based on  $D_{i,1}$  and  $D_{i,2}$ , respectively, in (3) or (4).

The problem fits the framework of alternating direction methods [33]. For simplicity, we let

$$f_1(X) = \frac{1}{2} \|HXA - Y\|_F^2$$

and

$$f_2\left(\begin{bmatrix} W^{(1)} & W^{(2)} & V \end{bmatrix}\right) = \chi_{\mathcal{K}}(V) + \mu_2 \sum_{i=1}^n \sum_{j=1}^m \|W_{i,j}\|_2 + \mu_1 \|V\|_{1,1}$$

where

$$\chi_{\mathcal{K}}(V) = \begin{cases} 0, & \text{if } V \in \mathcal{K} \\ \infty, & \text{otherwise.} \end{cases}$$

The constraints are expressed as follows:

$$BX + C\begin{bmatrix} W^{(1)} & W^{(2)} & V \end{bmatrix} := \begin{bmatrix} D_1 \\ D_2 \\ I_{n \times n} \end{bmatrix} X - I_{3n \times 3n} \begin{bmatrix} W^{(1)} \\ W^{(2)} \\ V \end{bmatrix} = 0_{3n \times m}$$

where  $I_{j \times j}$  is the  $j$ -by- $j$  identity matrix. The optimization problem in (5) is well structured since both sets of variables  $X$  and  $\begin{bmatrix} W^{(1)} & W^{(2)} & V \end{bmatrix}$  are separated. This allows one to solve  $X$  and  $\begin{bmatrix} W^{(1)} & W^{(2)} & V \end{bmatrix}$  in two decoupled subproblems, but the convergence of the algorithm can still be guaranteed [33]. For simplicity, we use  $Z$  to denote  $\begin{bmatrix} W^{(1)} & W^{(2)} & V \end{bmatrix}$  in the following discussion.

By attaching the Lagrangian multiplier

$$\Lambda = \begin{bmatrix} \Lambda^{(1)} \\ \Lambda^{(2)} \\ \Lambda^{(3)} \end{bmatrix} \in \mathbb{R}^{3n \times m}$$

to the linear constraints, the augmented Lagrangian function of (5) is given by

$$L(X, Z, \Lambda) = f_1(X) + f_2(Z) + \langle \Lambda, BX + CZ \rangle + \frac{\beta}{2} \|BX + CZ\|_F^2 \quad (6)$$

where  $\beta > 0$  is the penalty parameter for the violation of the linear constraints and  $\langle \cdot, \cdot \rangle$  is the sum of the entries of the Hadamard product. More specifically, to approach a solution of (6), the alternating direction method solves the following subproblems at each iteration:

$$\begin{cases} \text{Step 1 : } X_{k+1} \in \arg \min L(X, Z_k, \Lambda_k) \\ \text{Step 2 : } Z_{k+1} \in \arg \min L(X_{k+1}, Z, \Lambda_k) \\ \text{Step 3 : } \Lambda_{k+1} = \Lambda_k + \beta(BX_{k+1} + CZ_{k+1}). \end{cases}$$

In Step 1, we solve the following subproblem:

$$X_{k+1} \in \arg \min \left\{ \frac{1}{2} \|HXA - Y\|_F^2 + \langle \Lambda_k, BX + CZ_k \rangle + \frac{\beta}{2} \|BX + CZ_k\|_F^2 \right\}. \quad (7)$$

$X^{k+1}$  is thus the solution of the classical Sylvester matrix equation

$$H^T H X A A^T + \beta B^T B X = H^T Y A^T - \beta B^T C Z_k - B^T \Lambda_k. \quad (8)$$

By using the Kronecker product notations, the aforementioned Sylvester matrix equation can be reformulated as the following form:

$$(A A^T \otimes H^T H + \beta I \otimes B^T B) \text{vec}(X) = \text{vec}(H^T Y A^T - \beta B^T C Z_k - B^T \Lambda_k) \quad (9)$$

where  $\text{vec}$  refers to a vector by the lexicographical ordering of the entries in a matrix. We note that the linear system in (9) can be solved efficiently by using singular value decomposition of  $A$  and the Fourier decomposition of  $H$  and  $B^T B$  with periodic boundary conditions

$$A = U \Sigma V^* \quad H = F^* \Gamma F \quad B^T B = F^* \Psi^2 F$$

where  $U$  and  $V$  are singular vectors of  $A$  and  $F$  is the 2-D discrete transform matrix. When  $B$  and  $H$  are with Neumann boundary conditions, both can be diagonalized by discrete cosine transform matrix; see [25] for more details. The cost of computing the singular value decomposition of  $A$  is  $O(m^2 l)$ , and the cost of computing Fourier decompositions of  $H$  and  $B^T B$  is  $O(n^2 \log n)$ .

From (9), we have

$$(U \otimes F^*)(\Sigma^2 \otimes \Gamma^2 + I \otimes \Psi^2)(U^* \otimes F) \text{vec}(X) = \text{vec}(H^T Y A^T - \beta B^T C Z_k - B^T \Lambda_k)$$

and thus, the solution  $\text{vec}(X)$  is explicitly given by

$$\text{vec}(X) = (U \otimes F^*)(\Sigma^2 \otimes \Gamma^2 + I \otimes \Psi^2)^{-1}(U^* \otimes F) \cdot \text{vec}(H^T Y A^T - \beta B^T C Z_k - B^T \Lambda_k). \quad (10)$$

The cost of computing  $\text{vec}(H^T Y A^T)$  is  $O(\ln \log n + lmn)$ , and  $\text{vec}(H^T Y A^T)$  needs to be computed only once. At each iteration, the cost of computing  $\text{vec}(\beta B^T C Z_k - B^T \Lambda_k)$  is  $O(mn)$  operations, and the cost of computing the product of the matrix  $(U^* \otimes F)$  (or  $(U \otimes F^*)$ ) with an  $mn$ -vector is  $O(nm^2 + mn \log n)$ . Therefore, the complexity of obtaining  $\text{vec}(X)$  is  $O(2nm^2 + mn \log n)$  at each iteration.

In Step 2, we solve the following subproblem:

$$Z_{k+1} \in \arg \min \left\{ \chi_{\mathcal{K}}(V) + \mu_2 \sum_{i=1}^n \sum_{j=1}^m \|W_{i,j}\|_2 + \mu_1 \|V\|_{1,1} + \langle \Lambda_k, BX_{k+1} + CZ \rangle + \frac{\beta}{2} \|BX_{k+1} + CZ\|_F^2 \right\}. \quad (11)$$

Since the variables  $\begin{bmatrix} W^{(1)} & W^{(2)} \end{bmatrix}$  and  $V$  are decoupled, their optimal solutions for (11) can be determined separately as follows:

$$\begin{bmatrix} W_{k+1}^{(1)} & W_{k+1}^{(2)} \end{bmatrix} \in \arg \min \left\{ \frac{\beta}{2} \left\| \begin{bmatrix} W^{(1)} \\ W^{(2)} \end{bmatrix} - \begin{bmatrix} D^{(1)} X_{k+1} \\ D^{(2)} X_{k+2} \end{bmatrix} - \frac{1}{\beta} \begin{bmatrix} \Lambda_k^{(1)} \\ \Lambda_k^{(2)} \end{bmatrix} \right\|_F^2 + \sum_{i=1}^n \sum_{j=1}^m \|W_{i,j}\|_2 \right\} \quad (12)$$

and

$$V_{k+1} \in \arg \min_{V \geq 0} \left\{ \mu_1 \|V\|_{1,1} + \frac{\beta}{2} \left\| V - X_{k+1} - \frac{1}{\beta} \Lambda_k^{(3)} \right\|_F^2 \right\}. \quad (13)$$

We note from (12) that each  $W_{i,j}$  can be determined independently by solving  $nm$  two-variable minimization problems

$$\begin{aligned} \min_{W_{i,j}^{(1)}, W_{i,j}^{(2)}} & \left\{ \mu_2 \sqrt{|W_{i,j}^{(1)}|^2 + |W_{i,j}^{(2)}|^2} \right. \\ & + \frac{\beta}{2} \left[ W_{i,j}^{(1)} - \left( D^{(1)} X_{k+1} \right)_{i,j} - \frac{1}{\beta} \left( \Lambda_k^{(1)} \right)_{i,j} \right]^2 \\ & \left. + \frac{\beta}{2} \left[ W_{i,j}^{(2)} - \left( D^{(2)} X_{k+1} \right)_{i,j} - \frac{1}{\beta} \left( \Lambda_k^{(2)} \right)_{i,j} \right]^2 \right\}. \end{aligned} \quad (14)$$

The solution can be given explicitly by using the well-known 2-D shrinkage formula [34] as follows:

$$\left[ W_{i,j}^{(1)}, W_{i,j}^{(2)} \right] = \max \left\{ \|P_{i,j}\|_2 - \frac{\mu_2}{\beta}, 0 \right\} \frac{P_{i,j}}{\|P_{i,j}\|_2} \quad (15)$$

for  $1 \leq i \leq n$  and  $1 \leq j \leq m$ , where

$$P_{i,j} := \left[ \left( D^{(1)} X_{k+1} \right)_{i,j} + \frac{1}{\beta} \left( \Lambda_k^{(1)} \right)_{i,j}, \left( D^{(2)} X_{k+1} \right)_{i,j} + \frac{1}{\beta} \left( \Lambda_k^{(2)} \right)_{i,j} \right]$$

for  $1 \leq i \leq n$  and  $1 \leq j \leq m$ , where  $0 \cdot (0/0) = 0$  is followed. The cost of computing  $[W^{(1)}, W^{(2)}]$  is  $O(nm)$ .

For (13), we use a similar trick to obtain the solution. However, each  $V_{i,j}$  is required to be nonnegative in the optimization problem. Therefore, the optimal solution of (13) is given by

$$V_{i,j} = \max \left\{ \|Q_{i,j}\|_2 - \frac{\mu_2}{\beta}, 0 \right\}, \quad 1 \leq i \leq n; \quad 1 \leq j \leq m \quad (16)$$

where

$$Q_{i,j} := (X_{k+1})_{i,j} + \frac{1}{\beta} \left( \Lambda_k^{(3)} \right)_{i,j}, \quad 1 \leq i \leq n; \quad 1 \leq j \leq m.$$

The cost of computing  $V$  is  $O(nm)$ .

We see that every step of the alternating direction method has an explicit solution: The ADM method is thus efficiently implementable. At each iteration, the cost of computing all the variables  $X$ ,  $[W^{(1)}, W^{(2)}]$ , and  $V$  at Steps 1–3 in the optimization problem is  $O(2nm^2 + mn \log n)$ . On the other hand, the convergence of the alternating direction method for convex objective functions of separable variables with linear constraints is guaranteed; see, for instance, [32], [33], and [35]. In particular, (5) satisfies the required convergence conditions, and thus, the iterative method in Steps 1–3 can give the optimal solution of (5). In the following, we provide several remarks on features of the proposed numerical scheme.

*Remark 1:* In the aforementioned proposed algorithm, we consider the isotropic TV in (4). We can easily modify the algorithm to handle the anisotropic TV in (3). More precisely, we study the following optimization problem:

$$\begin{aligned} \min_{V, W, X} & \mu_2 \sum_{i=1}^n \sum_{j=1}^m \|W_{i,j}\|_1 + \mu_1 \|V\|_{1,1} + \frac{1}{2} \|HXA - Y\|_F^2 \\ \text{subject to} & \\ & D_1 X = W^{(1)} \quad D_2 X = W^{(2)} \quad V = X \\ & V \in \mathcal{K} := \{V \in \mathbb{R}^{n \times m}, V \geq 0\}. \end{aligned} \quad (17)$$

Similar algorithm can be derived for solving the optimization problem (17). The  $X$ -subproblem can be solved by (9), and the closed-form solution is given by (10). The  $Z$ -subproblem can be solved as follows:

$$\begin{aligned} Z_{k+1} \in \arg \min & \left\{ \chi_{\mathcal{K}}(V) + \mu_2 \sum_{i=1}^n \sum_{j=1}^m \|W_{i,j}\|_1 + \mu_1 \|V\|_{1,1} \right. \\ & \left. + \langle \Lambda_k, BX_{k+1} + CZ \rangle + \frac{\beta}{2} \|BX_{k+1} + CZ\|_F^2 \right\}. \end{aligned}$$

For the variables  $[W^{(1)}, W^{(2)}]$ , they are given by

$$\begin{aligned} [W_{k+1}^{(1)}, W_{k+1}^{(2)}] \in \arg \min & \left\{ \frac{\beta}{2} \left\| \begin{pmatrix} W^{(1)} \\ W^{(2)} \end{pmatrix} \right\|_F^2 \right. \\ & \left. - \left\| \begin{pmatrix} D^{(1)} X_{k+1} \\ D^{(2)} X_{k+1} \end{pmatrix} - \frac{1}{\beta} \begin{pmatrix} \Lambda_k^{(1)} \\ \Lambda_k^{(2)} \end{pmatrix} \right\|_F^2 + \sum_{i=1}^n \sum_{j=1}^m \|W_{i,j}\|_1 \right\} \end{aligned}$$

and the solution can be given explicitly as follows:

$$W_{i,j}^{(1)} = \max \left\{ \left| \left( D^{(1)} X_{k+1} \right)_{i,j} + \frac{1}{\beta} \left( \Lambda_k^{(1)} \right)_{i,j} \right| - \frac{\mu_2}{\beta}, 0 \right\} \cdot \frac{\left( D^{(1)} X_{k+1} \right)_{i,j} + \frac{1}{\beta} \left( \Lambda_k^{(1)} \right)_{i,j}}{\left| \left( D^{(1)} X_{k+1} \right)_{i,j} + \frac{1}{\beta} \left( \Lambda_k^{(1)} \right)_{i,j} \right|}$$

and

$$W_{i,j}^{(2)} = \max \left\{ \left| \left( D^{(2)} X_{k+1} \right)_{i,j} + \frac{1}{\beta} \left( \Lambda_k^{(2)} \right)_{i,j} \right| - \frac{\mu_2}{\beta}, 0 \right\} \cdot \frac{\left( D^{(2)} X_{k+1} \right)_{i,j} + \frac{1}{\beta} \left( \Lambda_k^{(2)} \right)_{i,j}}{\left| \left( D^{(2)} X_{k+1} \right)_{i,j} + \frac{1}{\beta} \left( \Lambda_k^{(2)} \right)_{i,j} \right|}$$

for  $1 \leq i \leq n$  and  $1 \leq j \leq m$ . On the other hand, the variables  $V_{k+1}$  are given by the same formula in (16).



At each iteration, the cost of computing all the variables  $X$ ,  $[W^{(1)}, W^{(2)}]$ , and  $V$  in this optimization problem is  $O(2nm^2 + mn \log n)$ .

*Remark 2:* The proposed numerical scheme is different from the SUnSAL-TV method which employs anisotropic TV (as mentioned in [21]). We note that two auxiliary variables are coupled together in the SUnSAL-TV method,<sup>1</sup> and therefore, the theoretical convergence of the alternating direction method cannot be guaranteed even if the results show the numerical convergence. Moreover, more computational steps are required in the SUnSAL-TV method; we find in the numerical results of the next section that the SUnSAL-TV method converges more slowly than the proposed method.

Iordache *et al.* [21] introduced six matrix variables to decouple the optimization problem, while the proposed numerical scheme only requires four matrix variables ( $n$ -by- $m$  matrix  $X$ ,  $n$ -by- $m$  matrix  $W_1$ ,  $n$ -by- $m$  matrix  $W_2$ , and  $n$ -by- $m$  matrix  $V$ ) and the  $m$ -by- $m$  matrix decomposition variable  $U$ . The storage cost of the proposed numerical method is  $4mn + m^2$ . It is stated in [21] that there are six matrix variables<sup>2</sup> and the  $m$ -by- $l$  matrix decomposition of the coefficient matrix in the first step of the SUnSAL-TV method; thus, the storage cost is  $6mn + ln + lm$ . On the other hand, the computational complexity of the SUnSAL-TV method per iteration is  $O(mn \log n + 2mnl)$ ,<sup>3</sup> which is lower than that of the proposed method per iteration,  $O(2nm^2 + mn \log n)$  when  $m > l$ .

However, in the numerical results of using the real hyperspectral libraries,  $m$  and  $l$  have the same order of magnitude, and  $n$  is significantly larger than both  $m$  and  $l$ . The storage cost of the proposed method is less than that required in the SUnSAL-TV method, and the computational complexity of the SUnSAL-TV method is not significantly less than that of the proposed method.

*Remark 3:* The modified alternating minimization scheme is employed for compressive sensing and unmixing of hyperspectral data by the authors of [24]. The  $X$ -subproblem was not exactly solved in their proposed algorithm even without deblurring, while the key step of our numerical scheme is the transformation from the matrix equation (8) to the linear system which has a closed-form solution (10).

### III. EXPERIMENTAL RESULTS

In this section, we test the proposed algorithm for deblurring and unmixing model using anisotropic and isotropic TV regularization. Both simulated and real hyperspectral data are generated to evaluate the efficiency and effectiveness of the proposed algorithm. The quality of the estimated fractional

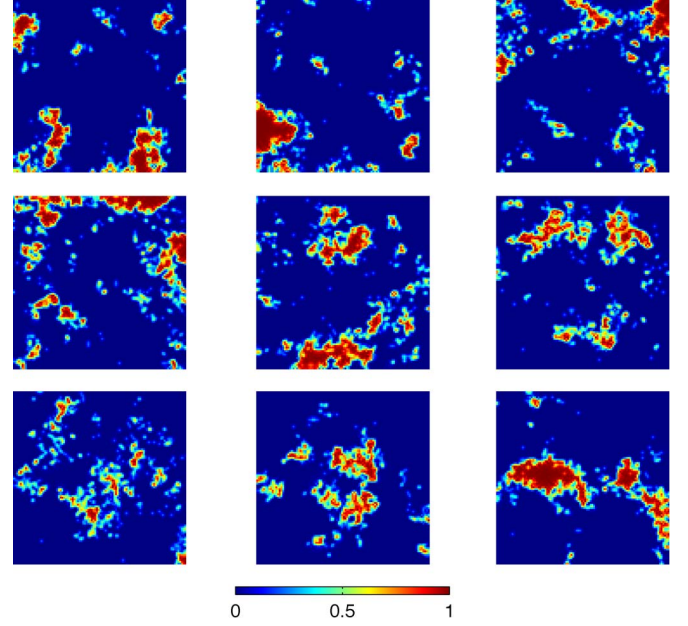


Fig. 1. True fractional abundance maps of selected endmembers in Example 1.

abundances of endmembers is evaluated by using the signal-to-reconstruction error (SRE) defined by

$$\text{SRE} := \frac{\mathbb{E} \left[ \|X_{\text{true}}\|_F^2 \right]}{\mathbb{E} \left[ \|X_{\text{true}} - \hat{X}\|_F^2 \right]}$$

measured in decibels, where  $\mathbb{E}$  denotes the expected value; see also [21]. Here,  $X_{\text{true}}$  denotes the true fractional abundances of endmembers, and  $\hat{X}$  is the computed fractional abundances of endmembers by the proposed algorithm. We adopt

$$\frac{\|X_k - X_{k-1}\|_F}{\|X_{k-1}\|_F} < 10^{-3}$$

as the same stopping criterion of the SUnSAL-TV method and for the proposed method for a fair comparison. The MATLAB code of the SUnSAL-TV method, which employs anisotropic TV, is used and given in [21]. We also implement the proposed method using the MATLAB code. All the tests are performed under Windows XP and Matlab Version 7.10 (R2010a) running on a desktop with an Intel(R) Xeon(R) CPU E5504 at 2.00 GHz and 48.0 GB of memory.

#### A. Example 1

In this example, we first generate a spectral library matrix  $A \in \mathbb{R}^{120 \times 100}$ , using a library of 262 spectral signatures generally found on satellites, from the National Aeronautics and Space Administration Johnson Space Center (NASA JSC) Spacecraft Materials Spectral Database, NASA JSC [36], [38], [39], with 100 spectral bands. This real database has also been used in [23] and [27]. Nine signatures are randomly chosen, and a  $100 \times 100$  pixels datacube of true observations is generated. The true fractional abundances of nine piecewise

<sup>1</sup>In [21], both auxiliary variables  $V_3$  and  $V_4$  (the notations used in [21]) are coupled together.

<sup>2</sup>The variables are  $m$ -by- $n$   $U$ ,  $l$ -by- $n$   $V_1$ ,  $m$ -by- $n$   $V_2$ ,  $m$ -by- $n$   $V_3$ ,  $2m$ -by- $n$   $V_4$ , and  $m$ -by- $n$   $V_5$  (the notations used in [21]).

<sup>3</sup>By using the notations in [21], the first step precomputes the matrix decomposition of an  $m$ -by- $m$  matrix  $(A^T A + 3I)$  in  $O(l^2 m)$  with  $l$ -by- $m$  matrix  $A$  and  $m > l$ , and the solution of the first step is  $O(2mnl)$  by computing  $(A^T A + 3I)^{-1}(A^T \xi_1 + \xi_2 + \xi_4 + \xi_5)$  via the matrix decomposition, where  $\xi_1$  is  $l$ -by- $n$  and  $\xi_2, \xi_4$ , and  $\xi_5$  are  $m$ -by- $n$  matrices. The second, third, fourth, fifth, and sixth steps are  $O(mnl)$ ,  $O(mn)$ ,  $O(mn \log n)$ ,  $O(mn)$ , and  $O(mn)$ , respectively.

TABLE I  
RESULTS USING  $TV_a$  AND  $TV_i$  FOR NOISE LEVELS OF (TOP) 30 AND (BOTTOM) 40 dB

		Our scheme ( $TV_a$ )			Our scheme ( $TV_i$ )			SUnSAL-TV		
$\mu_1$	$\mu_2$	SRE	Iter	Time	SRE	Iter	Time	SRE	Iter	Time
0	0	5.6019	166	564.36	5.6019	166	602.97	4.7604	468	1486.05
	$5 \times 10^{-5}$	5.8302	153	529.62	5.7906	154	571.95	5.0626	386	1260.25
	$5 \times 10^{-4}$	7.1494	128	442.83	6.9394	125	464.06	7.0955	354	1174.55
	$5 \times 10^{-3}$	9.2660	117	407.94	9.4616	116	431.41	9.4056	493	1563.50
0.0001	0	5.6255	165	565.75	5.6255	165	598.73	4.7546	448	1449.50
	$5 \times 10^{-5}$	5.8557	152	501.42	5.8153	153	569.03	5.0756	377	1288.64
	$5 \times 10^{-4}$	7.2111	127	416.05	6.9979	125	467.78	7.1567	344	1190.58
	$5 \times 10^{-3}$	9.3426	116	388.89	9.561	116	437.61	9.5073	479	1632.19
0.001	0	5.8724	164	566.00	5.8724	164	596.23	4.9877	428	1393.25
	$5 \times 10^{-5}$	6.1409	152	515.47	6.093	153	573.25	5.3488	357	1210.61
	$5 \times 10^{-4}$	7.8172	126	416.75	7.5693	124	464.66	7.9319	328	1118.84
	$5 \times 10^{-3}$	10.0244	113	380.47	10.3852	114	434.23	10.1032	465	1568.84
0.01	0	8.1191	143	479.22	8.1191	143	500.98	7.3239	520	1658.47
	$5 \times 10^{-5}$	8.4931	130	426.06	8.4291	131	484.63	7.8004	437	1491.39
	$5 \times 10^{-4}$	10.513	106	352.17	10.2494	104	382.83	10.6128	415	1421.97
	$5 \times 10^{-3}$	<b>12.9652</b>	96	357.17	<b>13.6333</b>	93	339.73	<b>12.9245</b>	462	1555.83

		Our scheme ( $TV_a$ )			Our scheme ( $TV_i$ )			SUnSAL-TV		
$\mu_1$	$\mu_2$	SRE	Iter	Time	SRE	Iter	Time	SRE	Iter	Time
0	0	9.7106	138	467.77	9.7106	138	506.25	9.3472	618	1976.86
	$5 \times 10^{-5}$	11.6442	99	344.05	11.3781	94	349.11	12.2661	527	1680.66
	$5 \times 10^{-4}$	<i>15.4527</i>	79	273.61	<i>15.8567</i>	67	247.52	<i>15.5197</i>	699	2240.45
	$5 \times 10^{-3}$	11.6995	150	517.00	12.57	110	406.05	11.7074	1845	6007.00
0.0001	0	9.9588	137	469.20	9.9588	137	504.77	9.6579	657	2127.27
	$5 \times 10^{-5}$	12.0349	99	343.59	11.7523	94	351.47	12.8599	503	1639.67
	$5 \times 10^{-4}$	15.9701	79	279.02	16.51	66	247.67	16.1130	650	2109.08
	$5 \times 10^{-3}$	11.8296	149	511.34	12.743	109	408.77	11.8267	1825	6031.91
0.001	0	11.8884	122	421.16	11.8884	122	434.13	11.9338	1043	3322.22
	$5 \times 10^{-5}$	14.4922	85	286.34	14.1747	80	296.17	15.2068	722	2337.36
	$5 \times 10^{-4}$	<b>18.4036</b>	77	260.47	<b>19.4019</b>	61	226.31	<b>19.0333</b>	603	1940.66
	$5 \times 10^{-3}$	12.8714	142	481.89	14.1009	101	373.25	12.7765	1694	5642.31
0.01	0	14.0054	235	780.45	14.0054	235	826.08	13.9290	453	1431.95
	$5 \times 10^{-5}$	14.9532	190	635.28	14.7251	176	649.83	15.0154	1548	5177.41
	$5 \times 10^{-4}$	17.1017	162	535.52	16.5246	136	505.95	17.3827	1430	4673.77
	$5 \times 10^{-3}$	15.2714	173	573.33	15.8829	134	489.70	16.2814	411	1306.91

smooth endmembers used and tested in [20] are shown in Fig. 1. A Gaussian white noise (noise level of 30 or 40 dB) is further added to the datacube. In Table I, we list the unmixing results by using the proposed algorithm for different values of parameters. In the table, the best results by using TV and sparsity regularization are shown in boldfaced style, while the best results by using TV regularization only are shown in italic style. Here, we remark that the results with the best SRE value are presented in Table I after many experiments with different values of penalty parameter  $\beta$ :  $10^{-3}$ ,  $10^{-2}$ ,  $10^{-1}$ , and 1. It is clear that the use of TV and sparsity regularization provides higher SRE results (about 4 dB) than the use of TV regularization only. It is interesting to note in these cases that the number of iterations of the alternating direction method when both TV and sparsity regularization are used is even less than that when using TV regularization only. We expect that the additional sparsity constraints force the method to obtain the optimizer and to converge quickly. We see from Table I and Fig. 2 that the results by using the anisotropic and isotropic TVs are not significantly different in terms of SRE and visual inspection.

In Table I, we also compare the performance of the proposed method with that of the SUnSAL-TV method. We see that the SUnSAL-TV method requires more iterations for convergence, and the computational time required by the SUnSAL-

TV method is more than that required by the proposed method to reach the same level of SRE values. To demonstrate the fast convergence of the proposed method, we show in Fig. 3 the convergence curves of the proposed method with anisotropic TV and the SUnSAL-TV method on SRE with respect to iterations. Here, we exhibit the convergence history of the proposed method with the same iteration number of the SUnSAL-TV method; the red circle in the figure denotes the real iteration number of the proposed method. It is clear that the convergence of the proposed method is faster than that of the SUnSAL-TV method for these tests. Moreover, the SRE values and running time results of different penalty parameters are reported in Table II for different noise levels of 30 dB ( $\mu_1 = 10^{-2}$  and  $\mu_2 = 5 \times 10^{-3}$ ) and 40 dB ( $\mu_1 = 10^{-3}$  and  $\mu_2 = 5 \times 10^{-4}$ ). The convergence of the proposed alternating direction method is theoretically guaranteed regardless of the penalty parameter as long as it is a positive number. In practice, we observe that the numerical performances of the proposed method and SUnSAL-TV method are affected by the value of penalty parameter.

Furthermore, we show the estimated fractional abundances of endmembers in the library for the first 120 pixels in Fig. 4 to appreciate the sparsity of fractional abundances. From Fig. 4, it can also be seen that the results are clearly improved when the sparsity term is imposed.

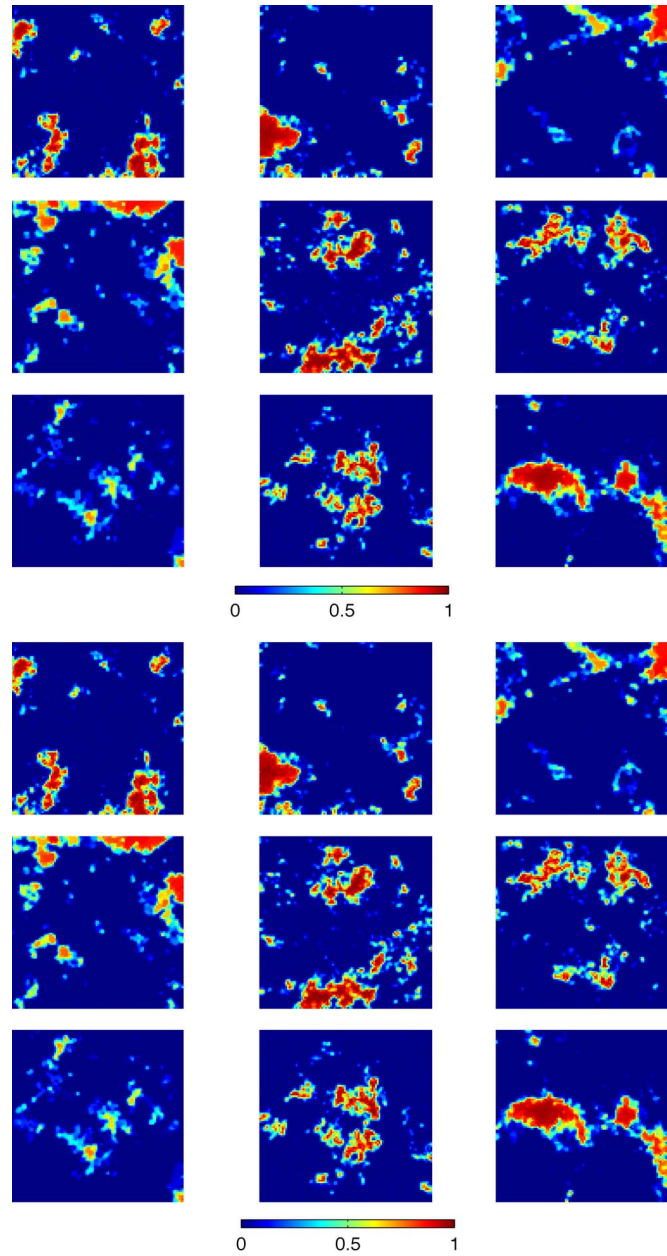


Fig. 2. Estimated fractional abundance maps using (top)  $TV_a$  and (bottom)  $TV_i$  for a noise level of 30 dB.

### B. Example 2

In the second example, we consider a simulated hyperspectral image of the Hubble Space Telescope, similar to those used in [23] and [27]. The data are a simulation of that collected by the U.S. Air Force AEOS Spectral Imaging Sensor (ASIS) which is used to collect adaptive optics compensated spectral images of astronomical objects and satellites at the Maui Space Surveillance Center [37] for space object surveillance. The key problem in nonresolved space object characterization is to use spectral reflectance data to gain knowledge regarding the physical properties (e.g., function, size, type, and status change) of space objects that cannot be spatially resolved with normal panchromatic telescope technology. Such objects may include geosynchronous satellites, rocket bodies, platforms, space debris, or nanosatellites. Spectral reflectance data of a

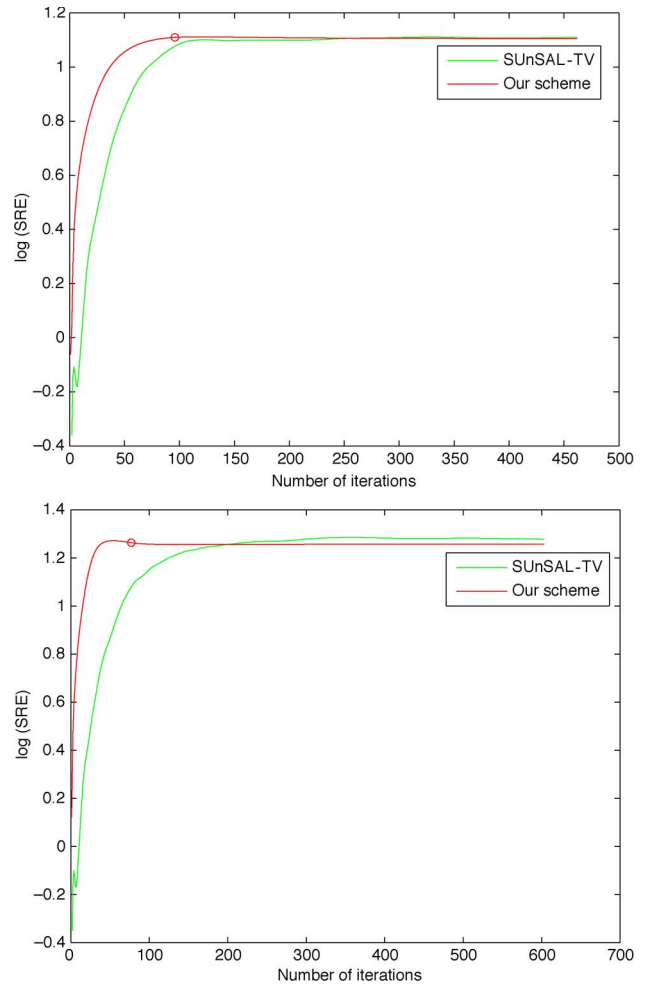


Fig. 3. Convergence curves of the proposed method with anisotropic TV and the SUnSAL-TV method for noise levels of (left) 30 and (right) 40 dB.

TABLE II  
RESULTS OF DIFFERENT PENALTY PARAMETERS FOR  
NOISE LEVELS OF (TOP) 30 AND (BOTTOM) 40 dB

	$\beta$	0	$10^{-1}$	$10^{-2}$	$10^{-3}$
Our scheme ( $TV_a$ )	SRE	9.044	12.9652	12.4719	10.6502
	Time	819.52	357.17	701.38	2672.48
SUnSAL-TV	SRE	6.5703	12.3914	12.9245	10.9710
	Time	1062.23	565.95	1555.83	3358.59
	$\beta$	0	$10^{-1}$	$10^{-2}$	$10^{-3}$
Our scheme ( $TV_a$ )	SRE	7.4308	16.1448	18.4036	16.8441
	Time	811.14	514.95	260.47	526.61
SUnSAL-TV	SRE	5.3134	13.2819	18.1418	19.0333
	Time	890.14	745.80	744.31	1940.66

space object can be gathered using ground-based spectrometers, such as the the ASIS system, located on the 3.67-m telescope at the Maui Space Surveillance Complex, and the data contain essential information regarding the makeup or types of materials comprising the object. Different materials, such as aluminum, Mylar, paint, plastics, solar cell, and other special materials, possess fairly unique characteristic wavelength-dependent absorption features or spectral signatures, which mix together in the spectral reflectance measurement of an object. The signatures cover a band of spectra from 0.4 to 2.5  $\mu\text{m}$  for 100 evenly distributed sampling points, leading to a hyperspectral



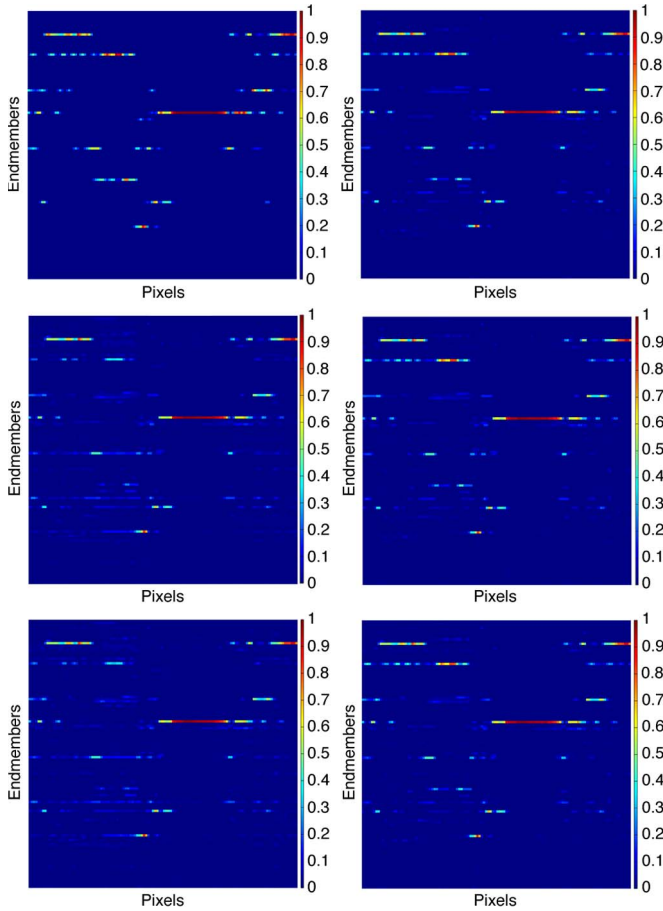


Fig. 4. (Upper leftmost) True fractional abundances. (Upper rightmost) Fractional abundances estimated by SUNSAL-TV. The fractional abundances estimated by our scheme using (second row)  $TV_a$  (left) without and (right) with sparsity. The fractional abundances estimated by our scheme using (third row)  $TV_i$  (left) without and (right) with sparsity for a noise level of 30 dB.

TABLE III  
MATERIALS, COLORS, AND CONSTITUENT ENDMEMBERS  
USED FOR THE SATELLITE SIMULATION

Material (color)	Constituent endmembers (%)
1 (blue)	Endmember 1 (100)
2 (brown)	Endmember 2 (70), Endmember 9 (30)
3 (red)	Endmember 3 (100)
4 (magenta)	Endmember 4 (60), Endmember 10 (40)
5 (green)	Endmember 5 (100)
6 (cyan)	Endmember 6 (40), Endmember 11 (30), Endmember 12 (30)
7 (yellow)	Endmember 7 (100)
8 (white)	Endmember 8 (100)

datacube of size  $128 \times 128 \times 100$ . In our simulation, there are eight materials. Their corresponding 12 endmembers are shown in Table III. The synthetic map of the satellite image is shown in Fig. 5. The hyperspectral datacube is blurred by a single Gaussian PSF (Matlab build-in function “fspecial” with  $s = 7$  and  $\rho = 0.7$ ) and then degraded by a Gaussian white noise of 30 or 40 dB. As an example, we show in Fig. 6 one band of the original hyperspectral image, the blurred hyperspectral image, and the blurred and noisy hyperspectral image.

The deblurring and unmixing results of SRE and the number of iterations are shown in Table IV. Again, the use of TV and sparsity regularization provides higher SRE results than the use

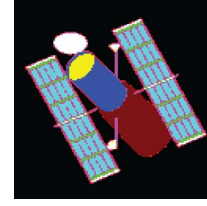


Fig. 5. Synthetic map of materials in Table III.



Fig. 6. One band of (left) the original hyperspectral image, (middle) the blurred hyperspectral image, and (right) the blurred and noisy hyperspectral image.

of TV regularization alone. We also observe that the improvement of the SRE results by both TV and sparsity regularization is more significant when blurring degrades the hyperspectral data. The estimated fractional abundances of chosen endmembers are shown in Figs. 7 and 8 under the 30-dB noise level setting. Their computational times are 621.65 and 585.34 s for the anisotropic and isotropic TV sparse models, respectively. It is clear that the results by using TV regularization only are not accurate. Also, we see from Table IV that the optimal deblurring and unmixing results by using the anisotropic and isotropic TVs are within 1 dB of each other. We see that the performance of using the anisotropic TV is slightly better than that of using the isotropic TV. However, their visual differences in Figs. 7 and 8 for the estimated fractional abundances of these two TVs are not obvious.

In Table V, we further show the relative errors between the estimated fractional abundances and the true fractional abundances of chosen endmembers for detailed performance evaluations of the deblurring and unmixing model. We can also observe from Table V the improvement of estimated fractional abundances by the use of sparsity regularization and TV regularization as compared with the use of TV regularization only.

### C. Example 3

In this example, we evaluate the performance of the proposed algorithm on a thematic map from the Center for Remote Imaging, Sensing and Processing at the National University of Singapore<sup>4</sup>; see Fig. 9. In the simulation, we associate different types of regions to ten endmembers in the thematic map; see Table VI. The size of the testing image is  $278 \times 329$ , and the number of bands to be considered is 100. Similarly, we generate a blurred and noisy datacube (Fig. 10) by using a Gaussian PSF and Gaussian white noise of 30 dB, similar to Example 2.

The true fractional abundances of ten randomly selected endmembers are given in Figs. 11 and 12. We search the parameters to obtain the highest SRE results. The resulting SRE

<sup>4</sup><http://www.crisp.nus.edu.sg/research/tutorial/process.htm>



TABLE IV  
RESULTS USING  $TV_a$  AND  $TV_i$  FOR NOISE LEVELS OF (LEFT) 30 AND (RIGHT) 40 dB

		$TV_a$		$TV_i$	
$\mu_1$	$\mu_2$	SRE	Iter	SRE	Iter
0	$5 \times 10^{-5}$	7.0545	177	6.8754	168
	$5 \times 10^{-4}$	8.8488	117	8.656	99
	$5 \times 10^{-3}$	6.6712	142	6.9015	109
0.0001	$5 \times 10^{-5}$	7.1798	177	6.9932	167
	$5 \times 10^{-4}$	8.9543	116	8.7761	98
	$5 \times 10^{-3}$	6.6807	143	6.9137	108
0.001	$5 \times 10^{-5}$	8.3701	162	8.139	154
	$5 \times 10^{-4}$	9.9204	97	9.8424	83
	$5 \times 10^{-3}$	6.7561	141	7.0066	105
0.01	$5 \times 10^{-5}$	9.9378	243	9.7376	237
	$5 \times 10^{-4}$	<b>12.1198</b>	194	<b>11.7075</b>	176
	$5 \times 10^{-3}$	7.4469	217	7.9301	210

		$TV_a$		$TV_i$	
$\mu_1$	$\mu_2$	SRE	Iter	SRE	Iter
0	$5 \times 10^{-5}$	13.6972	117	13.2035	113
	$5 \times 10^{-4}$	11.4199	87	11.5384	85
	$5 \times 10^{-3}$	6.7846	137	7.0259	104
0.0001	$5 \times 10^{-5}$	14.4618	120	13.8929	115
	$5 \times 10^{-4}$	11.5794	85	11.7499	84
	$5 \times 10^{-3}$	6.7940	138	7.0373	104
0.001	$5 \times 10^{-5}$	<b>19.5522</b>	118	<b>18.7844</b>	117
	$5 \times 10^{-4}$	13.1841	80	13.5294	75
	$5 \times 10^{-3}$	6.8599	138	7.1262	100
0.01	$5 \times 10^{-5}$	15.0172	194	14.696	191
	$5 \times 10^{-4}$	14.5006	186	14.2192	185
	$5 \times 10^{-3}$	7.5723	216	8.0766	206

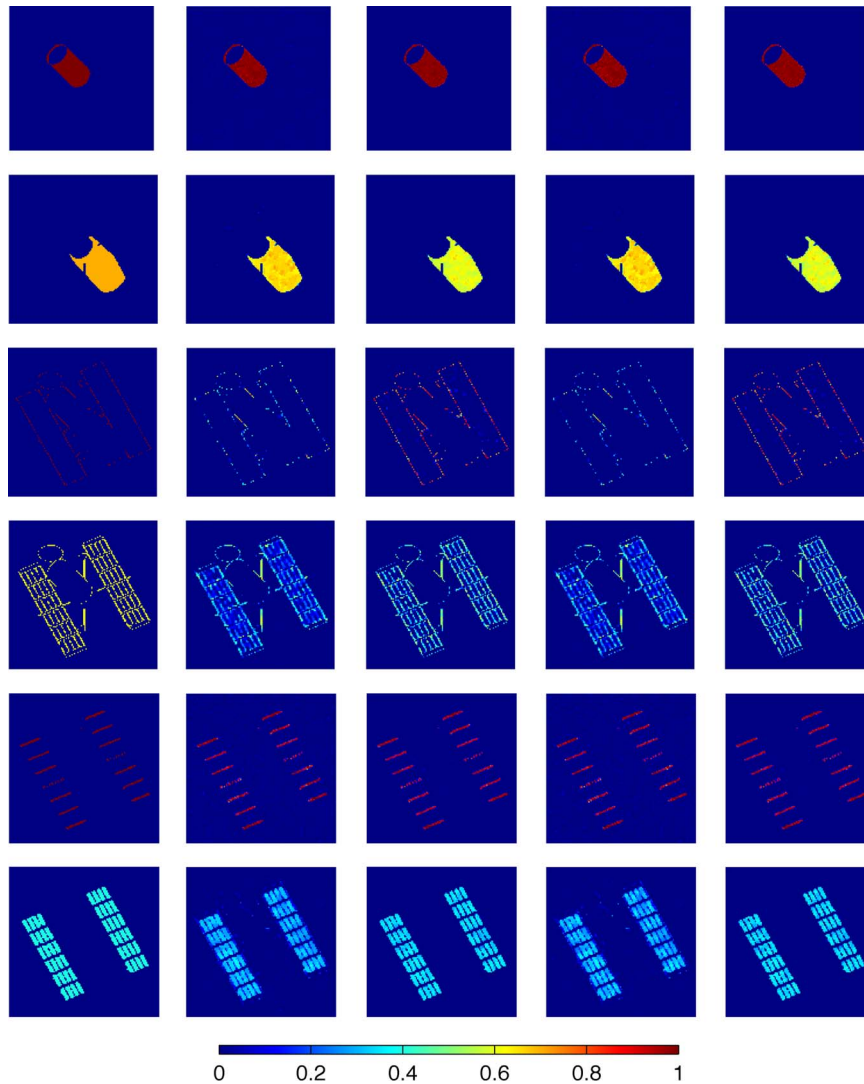


Fig. 7. Endmembers 1–6 in Example 2. (First column) True fractional abundances. The estimated fractional abundances by using  $TV_a$  (second column) without and (third column) with sparsity. The estimated fractional abundances by using  $TV_i$  (fourth column) without and (fifth column) with sparsity for a noise level of 30 dB.

(11.5530 dB with 134 iterations) of model (2) using both anisotropic TV ( $\mu_2 = 5 \times 10^{-4}$ ) and sparsity regularization ( $\mu_1 = 10^{-2}$ ) is higher than the resulting SRE (9.9398 dB with 152 iterations) of model (2) using the anisotropic TV only ( $\mu_1 = 0$  and  $\mu_2 = 5 \times 10^{-4}$ ). Their estimated fractional abundances of endmembers obtained are shown in Figs. 11 and 12. By visual inspection, we find that the estimated fractional

abundances by the proposed model are better than those by using the TV regularization only. In Table VII, the corresponding relative errors of the fractional abundances with respect to the true fractional abundances qualitatively validate this observation. We can safely conclude that the proposed deblurring and unmixing model is quite promising for deblurring and unmixing of hyperspectral data.

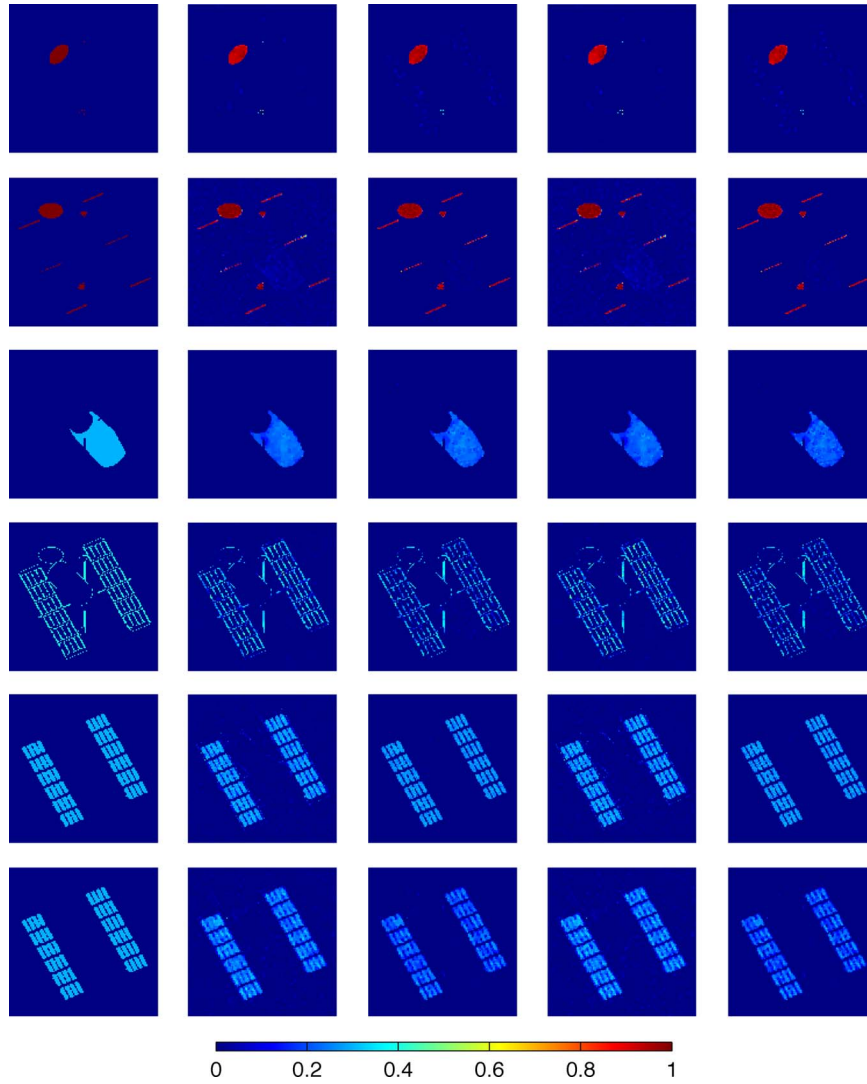


Fig. 8. Endmembers 7–12 in Example 2. (First column) True fractional abundances. The estimated fractional abundances by using  $TV_a$  (second column) without and (third column) with sparsity. The estimated fractional abundances by using  $TV_i$  (fourth column) without and (fifth column) with sparsity for a noise level of 30 dB.

TABLE V  
RELATIVE ERRORS OF THE ESTIMATED FRACTIONAL ABUNDANCES OF CHOSEN ENDMEMBERS FOR A NOISE LEVEL OF 30 dB

No.	$TV_a$ $\mu_1 = 0, \mu_2 = 5 \times 10^{-4}$	$TV_a$ $\mu_1 = 10^{-2}, \mu_2 = 5 \times 10^{-4}$	$TV_i$ $\mu_1 = 0, \mu_2 = 5 \times 10^{-4}$	$TV_i$ $\mu_1 = 10^{-2}, \mu_2 = 5 \times 10^{-4}$
Endmember 1	0.0400	0.0264	0.0455	0.0291
Endmember 2	0.0911	0.1597	0.1006	0.1706
Endmember 3	0.7426	0.2307	0.7736	0.2326
Endmember 4	0.5995	0.3760	0.5779	0.3861
Endmember 5	0.1256	0.1086	0.1317	0.1092
Endmember 6	0.3487	0.1880	0.3594	0.2069
Endmember 7	0.1125	0.1445	0.1216	0.1513
Endmember 8	0.1284	0.0783	0.1388	0.0821
Endmember 9	0.3131	0.3110	0.3413	0.3553
Endmember 10	0.3470	0.4367	0.3704	0.4683
Endmember 11	0.2628	0.1788	0.2798	0.1931
Endmember 12	0.4439	0.4418	0.4381	0.4486
average	0.2963	0.2234	0.3066	0.2361

#### D. Example 4

The well-known Airborne Visible/Infrared Imaging Spectrometer (AVIRIS) Cuprite data set<sup>5</sup> is considered in our real data experiment. The hyperspectral data used in experiments

correspond to a  $350 \times 350$  pixels subset with 188 spectral bands; see [6] and [21] for more details. We consider the  $240 \times 188$  spectral library generated from the USGS library<sup>6</sup> which includes all exposed minerals of interest. The mineral map is

<sup>5</sup><http://aviris.jpl.nasa.gov/html/aviris.freedata.html>

<sup>6</sup><http://speclab.cr.usgs.gov/spectral.lib06>

TABLE VI  
MATERIALS, COLORS, AND CONSTITUENT ENDMEMBERS USED FOR THE LANDSCAPE SIMULATION

Class No. (Color in Map)	Landcover Type	Constituent endmembers (%)
1 (black)	Clear water	Endmember 1 (60), Endmember 6 (40)
2 (green)	Dense Forest with closed canopy	Endmember 2 (90), Endmember 7 (10)
3 (yellow)	Shrubs, Less dense forest	Endmember 3 (50), Endmember 8 (50)
4 (orange)	Grass	Endmember 4 (100)
5 (cyan)	Bare soil, built-up areas	Endmember 5 (70), Endmember 9 (30)
6 (blue)	Turbid water, bare soil, built-up areas	Endmember 5 (30), Endmember 10 (40), Endmember 9 (30)
7 (red)	bare soil, built-up areas	Endmember 5 (50), Endmember 9 (50)
8 (white)	bare soil, built-up areas	Endmember 5 (40), Endmember 9 (60)

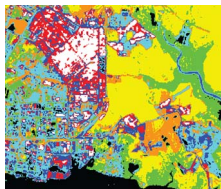


Fig. 9. Thematic map derived from the Satellite Pour l'Observation de la Terre image.



Fig. 10. One band of (left) the original hyperspectral image, (middle) the blurred hyperspectral image, and (right) the blurred and noisy hyperspectral image.

shown in Fig. 13, in which a Tricorder 3.3 software product was used to map different minerals present in the Cuprite district. Note that the publicly available AVIRIS Cuprite data were collected in 1997, while the Tricorder map was produced in 1995 by USGS. So, we only adopt the mineral map as a reference to evaluate the fractional abundance maps estimated by different methods. The estimated fractional abundance maps by the SUnSAL-TV method (701 iterations with 20030 s) and the proposed alternating direction method (410 iterations with 12153 s) are shown in Fig. 14. Even though all pixels in the Tricorder map are assumed to be pure pixels, it can be observed that, with less computational time, the proposed alternating direction method is generally able to find good approximations for fractional abundance maps of relevant minerals in the scene.

#### IV. CONCLUSIONS AND FURTHER WORK

We have presented a model containing both TV and sparsity regularization terms to deal with deblurring and unmixing of hyperspectral data. Experimental results have shown that the use of both TV and sparsity regularization terms is more effective than the use of TV regularization alone. We have developed an efficient algorithm to solve the proposed model and demonstrated that the numerical scheme is quite promising for deblurring and unmixing. The applications considered include space situational analysis and the analysis of natural thematic maps. Comparisons are made with the SUnSAL-TV method by Iordache *et al.* [21].

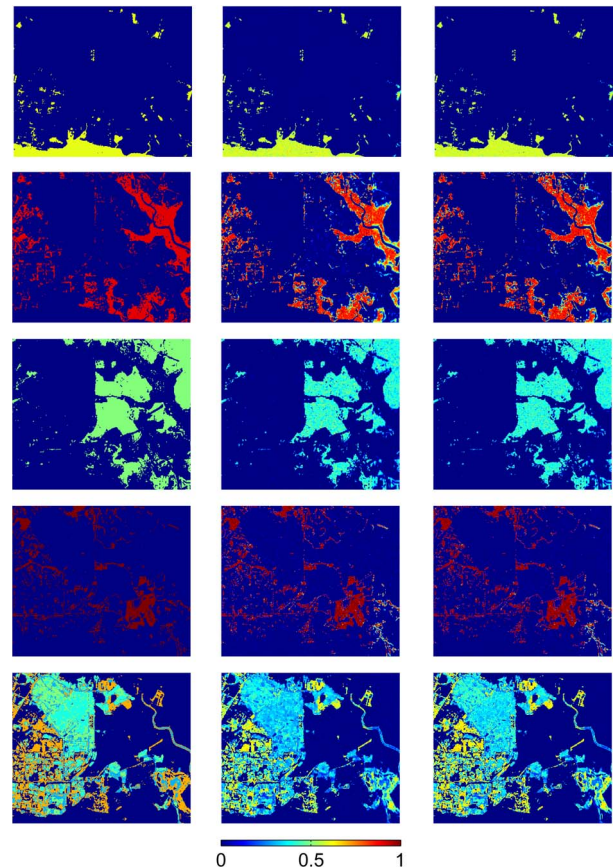


Fig. 11. Endmembers 1–5 in Example 3. (First column) True fractional abundance maps. The estimated fractional abundance maps by using  $TV_a$  (second column) without and (third column) with sparsity for a noise level of 30 dB.

In this paper, we have assumed that the PSF leading to the blurring matrix for hyperspectral data has already been estimated. In the next stage of our work, we plan to further investigate this topic. As discussed in Section I, hyperspectral image degradation is often “system dependent” [13]–[15], [30], [31], and the PSF of the image acquisition system needs to be identified. The system PSF relates generally to axial optical aberrations, while spatial PSFs relate to the usual image blurring problems such as defocus, motion, and imaging through a medium. Axial optical aberrations can lead to a significant blurring of image intensities in certain parts of the spectral range. These axial optical aberrations arise from the index of refraction variations that is dependent on the wavelength of incident light. In [13], the authors assumed a model of the PSF to be a “linear combination of Gaussian functions” across the different spectral bands; therefore, the overall PSF blur



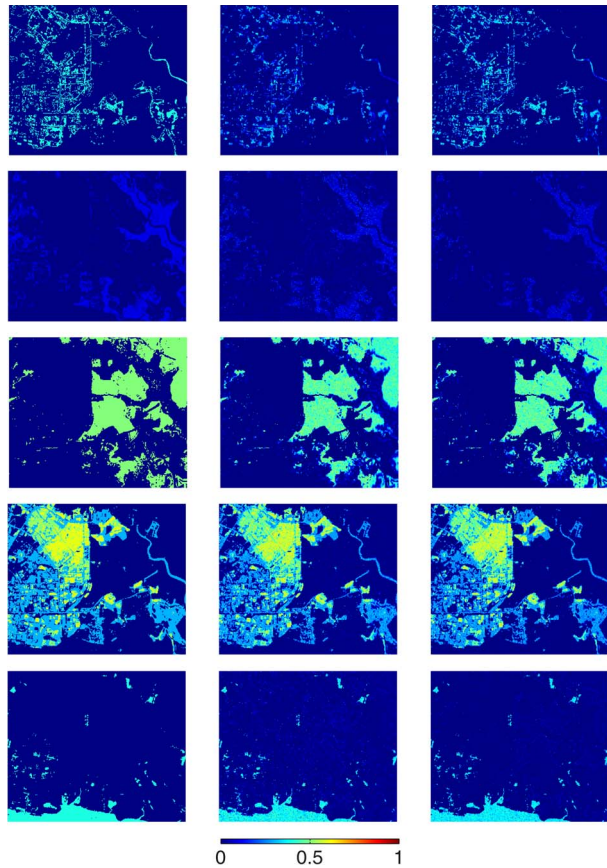


Fig. 12. Endmembers 6–10 in Example 3. (First column) True fractional abundance maps. The estimated fractional abundance maps by using  $TV_a$  (second column) without and (third column) with sparsity for a noise level of 30 dB.

TABLE VII  
RELATIVE ERRORS OF THE ESTIMATED FRACTIONAL ABUNDANCES  
OF CHOSEN ENDMEMBERS FOR A NOISE LEVEL OF 30 dB

No.	$TV_a$ $\mu_1 = 0$ $\mu_2 = 5 \times 10^{-4}$	$TV_a$ $\mu_1 = 10^{-2}$ $\mu_2 = 5 \times 10^{-4}$
Endmember 1	0.1312	0.1134
Endmember 2	0.2765	0.2467
Endmember 3	0.3041	0.3075
Endmember 4	0.1597	0.1396
Endmember 5	0.3005	0.2414
Endmember 6	0.6309	0.4307
Endmember 7	0.7063	0.6983
Endmember 8	0.2954	0.2730
Endmember 9	0.1782	0.1803
Endmember 10	0.3109	0.2556
average	0.3294	0.2887

identification process is reduced to finding only the corresponding scalar weight for each Gaussian function. We will follow a similar approach for fully estimating the overall system-dependent hyperspectral imaging PSF in our future work and will combine that process with the proposed deblurring and sparse unmixing method developed here.

#### ACKNOWLEDGMENT

The authors would like to thank the reviewers and the editors. They would also like to thank Prof. J. Bioucas-Dias (Instituto

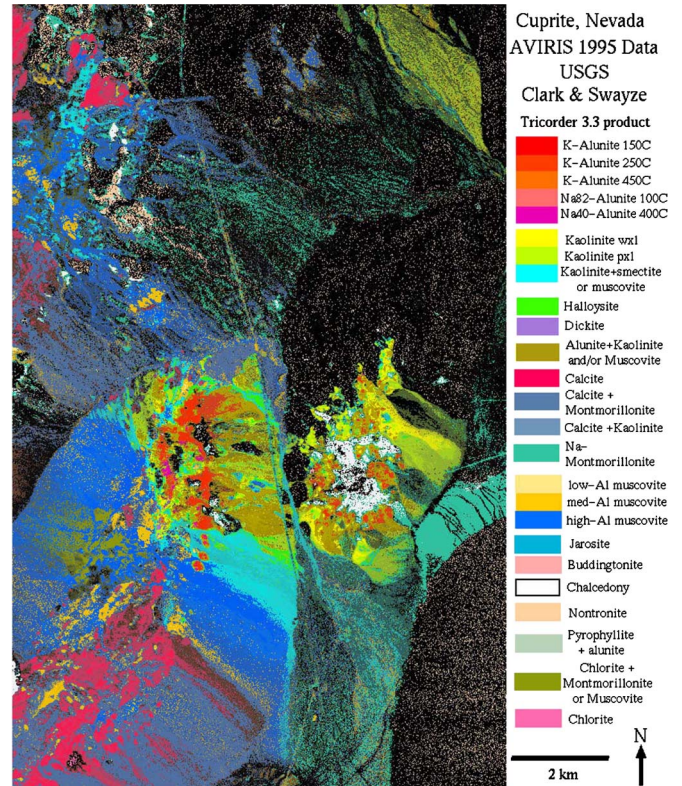


Fig. 13. USGS map showing the location of different minerals in the Cuprite mining district in Nevada.

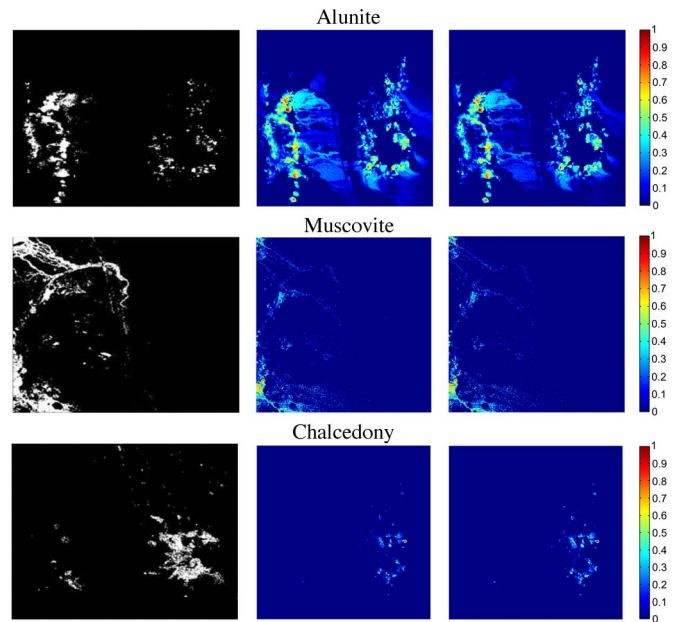


Fig. 14. (First column) Classification maps produced by the USGS Tricorder product, and the fractional abundance maps estimated by (second column) the SUnSAL-TV method and (third column) our scheme for the  $350 \times 350$  pixels subset of AVIRIS Cuprite scene.

Superior Técnico), M. Iordache (Universidad de Extremadura), K. Abercrombie (now with California Polytechnic State University), and Q. Zhang (Wake Forest University) for providing useful suggestions and hyperspectral data sets.



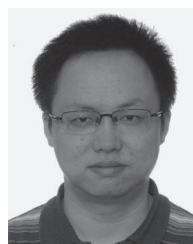
## REFERENCES

- [1] C. Chang, *Hyperspectral Imaging: Techniques for Spectral Detection and Classification*. New York: Plenum, 2003.
- [2] M. Eismann, *Hyperspectral Remote Sensing*. Bellingham, WA: SPIE, 2012.
- [3] J. Bioucas-Dias and J. Nascimento, "Hyperspectral subspace identification," *IEEE Trans. Geosci. Remote Sens.*, vol. 46, no. 8, pp. 2435–2445, Aug. 2008.
- [4] A. Zare and P. Gader, "PCE: Piecewise convex endmember detection," *IEEE Trans. Geosci. Remote Sens.*, vol. 48, no. 6, pp. 2620–2632, Jun. 2010.
- [5] F. Mianji and Y. Zhang, "SVM-Based unmixing-to-classification conversion for hyperspectral abundance quantification," *IEEE Trans. Geosci. Remote Sens.*, vol. 49, no. 11, pp. 4318–4327, Nov. 2011.
- [6] M. Iordache, J. Bioucas-Dias, and A. Plaza, "Sparse unmixing of hyperspectral data," *IEEE Trans. Geosci. Remote Sens.*, vol. 49, no. 6, pp. 2014–2039, Jun. 2011.
- [7] E. Hendrix, I. Garcia, J. Plaza, G. Martin, and A. Plaza, "A new minimum-volume enclosing algorithm for endmember identification and abundance estimation in hyperspectral data," *IEEE Trans. Geosci. Remote Sens.*, vol. 50, no. 7, pp. 2744–2757, Jul. 2012.
- [8] J. Bioucas-Dias, A. Plaza, N. Dobigeon, M. Parente, Q. Du, P. Gader, and J. Chanussot, "Hyperspectral unmixing overview: Geometrical, statistical, and sparse regression-based approaches," *IEEE J. Sel. Top. Appl. Earth Observ. Remote Sens.*, vol. 5, no. 2, pp. 354–379, Apr. 2012.
- [9] M. Winter, "N-FINDR: An algorithm for fast autonomous spectral end-member determination in hyperspectral data," in *Proc. SPIE Imaging Spectr. V*, 2003, vol. 3753, pp. 266–275.
- [10] J. Bioucas-Dias, "A variable splitting augmented Lagrangian approach to linear spectral unmixing," in *Proc. 1st WHISPERS*, 2009, vol. 1, pp. 1–4.
- [11] F. Schmidt, A. Schmidt, E. Tréguier, M. Guiheneuf, S. Moussaoui, and N. Dobigeon, "Implementation strategies for hyperspectral unmixing using Bayesian source separation," *IEEE Trans. Geosci. Remote Sens.*, vol. 48, no. 11, pp. 4003–4013, Nov. 2010.
- [12] J. Bioucas-Dias and M. Figueiredo, "Alternating direction algorithms for constrained sparse regression: Application to hyperspectral unmixing," in *Proc. 2nd WHISPERS*, 2010, vol. 1, pp. 1–4.
- [13] Z. Spiclin, F. Pernus, and B. Likar, "Correction of axial optical aberrations in hyperspectral imaging systems," in *Proc. SPIE*, 2011, vol. 7891, pp. 78910S–1–78910S–10.
- [14] M. Ng, R. Plemmons, and F. Pimentel, "A new approach to constrained total least squares image restoration," *Linear Algebra Appl.*, vol. 316, no. 1–3, pp. 237–258, Sep. 2000.
- [15] W. Wang and M. Ng, "On algorithms for automatic deblurring from a single image," *J. Comput. Math.*, vol. 30, no. 1, pp. 80–100, Jan. 2012.
- [16] D. Heinz and C. Chang, "Fully constrained least squares linear spectral mixture analysis method for material quantification in hyperspectral imagery," *IEEE Trans. Geosci. Remote Sens.*, vol. 39, no. 3, pp. 529–545, Mar. 2001.
- [17] N. Gillis and R. Plemmons, "Dimensionality reduction, classification and spectral mixture analysis using nonnegative underapproximation," *Opt. Eng.*, vol. 50, no. 2, pp. 027001–1–027001–16, Feb. 2011.
- [18] N. Gillis and R. Plemmons, "Sparse nonnegative matrix underapproximation and its application to hyperspectral image analysis," in *Proc. 3rd WHISPERS*, 2011, vol. 1, pp. 11–14.
- [19] Z. Guo, T. Wittman, and S. Osher, "L1 unmixing and its application to hyperspectral image enhancement," in *Proc. SPIE Conf. Algorithms Technol. Multispectral, Hyperspectral, Ultraspectral Imagery XV*, 2009, vol. 7334, pp. 73341M–1–73344M–9.
- [20] M. Iordache, J. Bioucas-Dias, and A. Plaza, "Total variation regularization in sparse hyperspectral unmixing," in *Proc. 3rd WHISPERS*, 2011, vol. 1, pp. 1–4.
- [21] M. Iordache, J. Bioucas-Dias, and A. Plaza, "Total variation spatial regularization for sparse hyperspectral unmixing," *IEEE Trans. Geosci. Remote Sens.*, vol. 50, no. 11, pp. 4484–4502, Nov. 2012.
- [22] M. Iordache, "A Sparse Regression Approach to Hyperspectral Unmixing," Ph.D. dissertation, Univ. Técnica de Lisboa, Lisboa, Portugal, 2011.
- [23] F. Li, M. Ng, and R. Plemmons, "Coupled segmentation and denoising/deblurring models for hyperspectral material identification," *Numer. Linear Algebra*, vol. 19, no. 1, pp. 153–173, Jan. 2012.
- [24] C. Li, T. Sun, K. Kelly, and Y. Zhang, "A compressive sensing and unmixing scheme for hyperspectral data processing," *IEEE Trans. Image Process.*, vol. 21, no. 3, pp. 1200–1210, Mar. 2012.
- [25] M. Ng, R. Chan, and W. Tang, "Fast algorithm for deblurring models with Neumann boundary conditions," *SIAM J. Sci. Comput.*, vol. 21, no. 3, pp. 851–866, Nov./Dec. 1999.
- [26] Q. Zhang, R. Plemmons, D. Kittle, D. Brady, and S. Prasad, "Joint segmentation and reconstruction of hyperspectral data with compressed measurements," *Appl. Opt.*, vol. 50, no. 22, pp. 4417–4435, Aug. 2011.
- [27] Q. Zhang, H. Wang, R. Plemmons, and V. Pauca, "Tensor methods for hyperspectral data analysis: A space object material identification study," *J. Opt. Soc. Amer. A, Opt. Image Sci.*, vol. 25, no. 12, pp. 3001–3012, Dec. 2008.
- [28] N. Joshi, R. Szeliski, and D. Kriegman, "PSF estimation using sharp edge prediction," in *Proc. IEEE Conf. CVPR*, 2008, vol. 1, pp. 1–8.
- [29] F. Chen and J. Ma, "An empirical identification method of Gaussian blur parameter for image deblurring," *IEEE Trans. Signal Process.*, vol. 57, no. 7, pp. 2467–2478, Jul. 2009.
- [30] T. Blake, S. Cain, M. Goda, and K. Jerkatis, "Model of the AEOS Spectral Imaging Sensor (ASIS) for spectral image deconvolution," in *Proc. AMOS Tech. Conf.*, Maui, HI, 2005.
- [31] E. Villeneuve, H. Carfantan, and D. Serre, "PSF estimation of hyperspectral data acquisition system for ground-based astrophysical observations," in *Proc. 3rd WHISPERS*, 2011, pp. 1–4.
- [32] M. Ng, W. Fan, and X. Yuan, "Inexact alternating direction methods for image recovery," *SIAM J. Sci. Comput.*, vol. 33, no. 4, pp. 1643–1668, Jul. 2011.
- [33] R. Glowinski, *Numerical Methods for Nonlinear Variational Problems*. New York: Springer-Verlag, 2008.
- [34] Y. Wang, J. Yang, W. Yin, and Y. Zhang, "A new alternating minimization algorithm for total variation image reconstruction," *SIAM J. Imaging Sci.*, vol. 1, no. 3, pp. 248–272, Jul. 2008.
- [35] J. Eckstein and D. Bertsekas, "On the Douglas–Rachford splitting method and the proximal point algorithm for maximal monotone operators," *Math. Program.*, vol. 55, no. 1, pp. 293–318, Jun. 1992.
- [36] K. Abercromby, Communication of the NASA JSC Spacecraft Materials Spectral Database, 2006.
- [37] T. Blake, S. Cain, M. Goda, and K. Jerkatis, "Reconstruction of spectral images from the AEOS Spectral Imaging Sensor," in *Proc. AMOS Tech. Conf.*, 2006, pp. E1–E22.
- [38] K. Jorgensen, J. Okada, J. Africano, D. Hall, M. Guyote, K. Hamada, G. Stansbery, E. Barker, and P. Kervin, "Reflectance spectra of human-made space objects," in *Proc. AMOS Tech. Conf.*, 2004, pp. 1–42.
- [39] T. Schildknecht, A. Vannanti, H. Krag, and C. Erd, "Reflectance spectra of space debris in GEO," in *Proc. AMOS Tech. Conf.*, 2009, pp. 220–227.



**Xi-Le Zhao** received the M.S. degree in computational mathematics from the University of Electronic Science and Technology of China, Chengdu, China, in 2009, where he is currently working toward the Ph.D. degree in the School of Mathematical Sciences.

In 2012, he was an exchange Ph.D. student at Hong Kong Baptist University, Kowloon Tong, Hong Kong. His research interests include the application of numerical linear algebra and sparse optimization in image processing.



**Fan Wang** received the B.S. and M.S. degrees from Lanzhou University, Lanzhou, China, and the Ph.D. degree from Hong Kong Baptist University (HKBU), Kowloon Tong, Hong Kong.

From 2004 to 2009, he was a Lecturer with the Department of Mathematics, Lanzhou University. In 2009, he joined the Institute for Computational Mathematics, HKBU. He is currently a Lecturer with the Department of Mathematics and Statistics, Lanzhou University. His main research activities are focused on image processing, numerical optimization, and numerical algebra.



**Ting-Zhu Huang** received the B.S., M.S., and Ph.D. degrees in computational mathematics from X'ian Jiaotong University, X'ian, China, in 1986, 1992, and 2000, respectively.

During 2005, he was a Visiting Scholar with the Department of Computer Science, Loughborough University, Loughborough, U.K. He is currently a Full Professor with the School of Mathematical Sciences, University of Electronic Science and Technology of China, Chengdu, China. He is currently an Editor of *Advances in Numerical Analysis*, the

*Journal of Pure and Applied Mathematics: Advances and Applications*, and the *Journal of Electronic Science and Technology of China*. His current research interests include numerical linear algebra with applications, iterative methods of linear systems and saddle point problems, preconditioning technologies, matrix analysis with applications, and computational electromagnetics.



**Michael K. Ng** received the B.Sc. and M.Phil. degrees from The University of Hong Kong, Hong Kong, in 1990 and 1992, respectively, and the Ph.D. degree from The Chinese University of Hong Kong, Shatin, Hong Kong, in 1995.

He is currently a Professor with the Department of Mathematics, Hong Kong Baptist University, Kowloon Tong, Hong Kong. He serves on the editorial boards of several international journals. His research interests include bioinformatics, data mining, image processing, scientific computing, and data

mining.



**Robert J. Plemmons** received the B.S. degree in mathematics and physics from Wake Forest University, Winston-Salem, NC, and the Ph.D. degree in applied mathematics from Auburn University, Auburn, AL.

In 1961–1965, he was a Professional Baseball Player with the Baltimore Orioles Farm System. In 1965, he was a Research Engineer with Martin Aerospace Company. In 1965–1967, he was a Research Scientist with the National Security Agency. In 1967–1981, he was with the Department of Math-

ematics and the Department of Computer Science, The University of Tennessee, Knoxville, where he was an Associate Professor and then a Professor. In 1981–1991, he was a Professor with the Department of Mathematics and the Department of Computer Science, North Carolina State University, Raleigh. He was a Visiting Professor at Stanford University, Stanford, CA (in 1978), the University of Illinois, Urbana (in 1986), the University of Minnesota, Minneapolis (in 1992), and Duke University, Durham, NC (in 1998). Since 1991, he has been a Z. Smith Reynolds Professor with the Department of Mathematics and the Department of Computer Science, Wake Forest University. His current research interests include scientific computation, specifically numerical linear algebra, ill-posed inverse problems, image processing, and hyperspectral and LiDAR methods in remote sensing, under funding from the Air Force Office of Scientific Research and the National Geospatial-Intelligence Agency.